The Astrophysical Journal, 948:95 (13pp), 2023 May 10 https://doi.org/10.3847/1538-4357/accc84

What Does the Geometry of the Hβ BLR Depend On?

Lizvette Villafaña[1], Peter R. Williams[1], Tommaso Treu[1], Brendon J. Brewer[2], Aaron J. Barth[3], Vivian U[3,4], Vardha N. Bennert[5], Hengxiao Guo[3,6], Misty C. Bentz[7], Gabriela Canalizo[4], Alexei V. Filippenko[8], Elinor Gates[9], Michael D. Joner[10], Matthew A. Malkan[1], Jong-Hak Woo[11,12], Bela Abolfathi[3], Thomas Bohn[4], K. Azalee Bostroem[13], Andrew Brandel[3], Thomas G. Brink[8], Sanyum Channa[14,15], Maren Cosens[16,17], Edward Donohue[5,18], Goni Halevi[8,19], Carol E. Hood[20], J. Chuck Horst[21], Maxime de Kouchkovsky[8], Benjamin Kuhn[21,22], Douglas C. Leonard[21], Raúl Michel[23], Melanie Kae B. Olaes[21], Daeseong Park[24,25], Jordan N. Runco[1], Remington O. Sexton[4,26,27], Isaac Shivvers[8], Chance L. Spencer[5,28], Benjamin E. Stahl[8,14], Samantha Stegman[8,29], Jonelle L. Walsh[30], and WeiKang Zheng[8]

[1] Department of Physics and Astronomy, University of California, Los Angeles, CA 90095-1547, USA; lvillafana@astro.ucla.edu
[2] Department of Statistics, The University of Auckland, Private Bag 92019, Auckland 1142, New Zealand
[3] Department of Physics and Astronomy, 4129 Frederick Reines Hall, University of California, Irvine, CA 92697-4575, USA
[4] Department of Physics and Astronomy, University of California, Riverside, CA 92521, USA
[5] Physics Department, California Polytechnic State University, San Luis Obispo, CA 93407, USA
[6] Key Laboratory for Research in Galaxies and Cosmology, Shanghai Astronomical Observatory, Chinese Academy of Sciences, 80 Nandan Road, Shanghai 200030, People's Republic of China
[7] Department of Physics and Astronomy, Georgia State University, Atlanta, GA 30303, USA
[8] Department of Astronomy, University of California, 501 Campbell Hall, Berkeley, CA 94720-3411, USA
[9] Lick Observatory, P.O. Box 85, Mt. Hamilton, CA 95140, USA
[10] Department of Physics and Astronomy, N283 ESC, Brigham Young University, Provo, UT 84602, USA
[11] Astronomy Program, Department of Physics and Astronomy, Seoul National University, 1 Gwanak-ro, Gwanak-gu, Seoul 08826, Republic of Korea
[12] SNU Astronomy Research Center, Seoul National University, 1 Gwanak-ro, Gwanak-gu, Seoul 08826, Republic of Korea
[13] DiRAC Institute, Department of Astronomy, University of Washington, 3910 15th Avenue, NE, Seattle, WA 98195, USA
[14] Department of Physics, University of California, Berkeley, CA 94720, USA
[15] Department of Physics, Stanford University, Stanford, CA 94305, USA
[16] Physics Department, University of California, San Diego, 9500 Gilman Drive, La Jolla, CA 92093, USA
[17] Center for Astrophysics and Space Sciences, University of California, San Diego, 9500 Gilman Drive, La Jolla, CA 92093, USA
[18] Booz Allen, 1615 Murray Canyon Road, Suite 8000, San Diego, CA 92108, USA
[19] Department of Astrophysical Sciences, Princeton University, 4 Ivy Lane, Princeton, NJ 08544, USA
[20] Department of Physics, California State University, San Bernardino, 5500 University Parkway, San Bernardino, CA 92407, USA
[21] Department of Astronomy, San Diego State University, San Diego, CA 92182-1221, USA
[22] Space Telescope Science Institute, 3700 San Martin Drive, Baltimore, MD 21218, USA
[23] Instituto de Astronomía, Universidad Nacional Autónoma de México, AP 877, Ensenada, Baja California, C.P. 22830, México
[24] Department of Astronomy and Atmospheric Sciences, Kyungpook National University, Daegu, 41566, Republic of Korea
[25] Korea Astronomy and Space Science Institute, Daejeon, 34055, Republic of Korea
[26] U.S. Naval Observatory, 3450 Massachusetts Ave NW, Washington, DC 20392-5420, USA
[27] Department of Physics and Astronomy, George Mason University, 4400 University Dr, Fairfax, VA 22030-4444, USA
[28] Department of Physics, California State University Fresno, Fresno, CA 93740-8031, USA
[29] Department of Chemistry, University of Wisconsin, Madison, WI 53706, USA
[30] George P. and Cynthia W. Mitchell Institute for Fundamental Physics and Astronomy, Department of Physics & Astronomy, Texas A&M University, 4242 TAMU, College Station, TX 77843, USA

Received 2022 May 23; revised 2023 April 6; accepted 2023 April 11; published 2023 May 11

Abstract

We combine our dynamical modeling black-hole mass measurements from the Lick AGN Monitoring Project 2016 sample with measured cross-correlation time lags and line widths to recover individual scale factors, f, used in traditional reverberation-mapping analyses. We extend our sample by including prior results from Code for AGN Reverberation and Modeling of Emission Lines (CARAMEL) studies that have utilized our methods. Aiming to improve the precision of black-hole mass estimates, as well as uncover any regularities in the behavior of the broad-line region (BLR), we search for correlations between f and other AGN/BLR parameters. We find (i) evidence for a correlation between the virial coefficient $\log_{10}(f_{\mathrm{mean},\sigma})$ and black-hole mass, (ii) marginal evidence for a similar correlation between $\log_{10}(f_{\mathrm{rms},\sigma})$ and black-hole mass, (iii) marginal evidence for an anticorrelation of BLR disk thickness with $\log_{10}(f_{\mathrm{mean,FWHM}})$ and $\log_{10}(f_{\mathrm{rms,FWHM}})$, and (iv) marginal evidence for an anticorrelation of inclination angle with $\log_{10}(f_{\mathrm{mean,FWHM}})$, $\log_{10}(f_{\mathrm{rms},\sigma})$, and $\log_{10}(f_{\mathrm{mean},\sigma})$. Last, we find marginal evidence for a correlation between line-profile shape, when using the root-mean-square spectrum, $\log_{10}(\mathrm{FWHM}/\sigma)_{\mathrm{rms}}$, and the virial coefficient, $\log_{10}(f_{\mathrm{rms},\sigma})$, and investigate how BLR properties might be related to line-profile shape using CARAMEL models.

Unified Astronomy Thesaurus concepts: Active galaxies (17); Active galactic nuclei (16); Seyfert galaxies (1447); Reverberation mapping (2019); Supermassive black holes (1663)

1. Introduction

It is widely accepted that most galaxies host a supermassive black hole in their center. When the black hole accretes material, it gives rise to a bright central source, known as an active galactic nucleus (AGN). Tight correlations between black-hole mass and host-galaxy properties (e.g., Magorrian et al. 1998; Ferrarese & Merritt 2000; Gebhardt et al. 2000; Kormendy & Ho 2013) suggest that AGNs play an important role in galaxy evolution. To understand such a link, both a better understanding of the central regions of AGNs and improved black-hole mass estimates are needed (Ding et al. 2020). Black-hole mass estimators applicable to cosmologically significant lookback times are particularly desirable, as they allow for the determination of the cosmic evolution of the galaxy black-hole mass correlations (e.g., Treu et al. 2004; Woo et al. 2006, 2008; Salviander et al. 2007; Shields & Salviander 2009; Bennert et al. 2010; Schulze & Wisotzki 2011; Targett et al. 2012; Ding et al. 2020).

Beyond our local universe, the black hole's gravitational sphere of influence cannot be spatially resolved with current technology, and thus dynamical black-hole mass measurements (e.g., modeling stellar/gas kinematics) cannot be constrained (Kormendy & Richstone 1995; Ferrarese & Ford 2005), with rare exceptions (e.g., 3C 273, IRAS 09149–6206; Gravity Collaboration et al. 2018, 2020). Instead, reverberation mapping is the primary tool used to estimate black-hole masses in the distant universe, with a limited application to broad-line (Type 1) AGNs.

The technique resolves the gravitational sphere of influence of the central black hole in time by utilizing variations in the continuum that are later reverberated by the broad emission lines (Blandford & McKee 1982; Peterson 1993; for a review, see Cackett et al. 2021). Assuming the delay in variations is due solely to light-travel time, the radius of the broad-line region (BLR) is measured by combining the observed time lag, τ, with the speed of light. A second key assumption, that BLR kinematics are dominated by the black hole's gravity, provides the velocity of the emitting gas, v, as determined by the width of the broad line. Combining the size of the BLR with its velocity, a virial constraint of the black hole's mass ($M_{\rm BH}$) is given by

$$M_{\rm BH} = f\frac{c\tau v^2}{G} = fM_{\rm vir}, \tag{1}$$

where f, or the "virial coefficient," is a dimensionless scale factor of order unity that captures the relation between measured line-shape parameters and BLR geometry/dynamics, and $c\tau v^2/G$ is referred to as the virial product ($M_{\rm vir}$).

In principle, construction of a velocity-delay map, which maps continuum variations to the broad-line flux variations as both a function of line-of-sight velocity and time delay, allows one to constrain the BLR geometry (Blandford & McKee 1982). In practice, however, interpretation is nontrivial, and much about the structure and kinematics of the BLR still remains unknown. For this reason, it is currently impossible to determine the scale factor for an individual AGN using traditional reverberation-mapping techniques. Instead, a constant average scale factor, found by aligning reverberation-mapped AGNs to the local $M_{\rm BH}$–σ_* relation, is often used for traditional reverberation-mapping black-hole mass estimates (Onken et al. 2004; Collin et al. 2006; Woo et al. 2010, 2013, 2015; Graham et al. 2011; Park et al. 2012a; Grier et al. 2013; Batiste et al. 2017).

Over the last several years, our team has set out to provide a more reliable way to calibrate the virial coefficient and uncover any regularity in BLR behavior. The discovery of any trends would thus provide both insight into the inner regions of AGNs and improve the way black-hole masses are calibrated across cosmic time.

Using the methods introduced by Pancoast et al. (2011), such as the Code for AGN Reverberation and Modeling of Emission Lines (CARAMEL), we explore a phenomenological description of the BLR and constrain a black-hole mass that is consistent with the reverberation-mapping data set, without the need of assuming a scale factor. In this paper, we combine our CARAMEL $M_{\rm BH}$ estimates for the nine sources modeled from the Lick AGN Monitoring Project 2016 (LAMP 2016; Villafaña et al. 2022, hereafter V22) with those from prior CARAMEL studies, and determine AGN-specific virial coefficients in order to search for a more reliable way to calibrate f.

This paper is organized as follows. We summarize the geometry and kinematics of the CARAMEL model in Section 2 and outline our methodology in calculating AGN-specific virial coefficients in Section 3. A systematic investigation of correlations between f and observables is carried out in Section 4. Specifically, we consider correlations with AGN/BLR model parameters in Section 4.1 and line-profile shape in Section 4.2. We then investigate the effects of BLR geometry and kinematics on BLR line-profile shape in Section 5 and summarize our main conclusions in Section 6.

2. Summary of Relevant CARAMEL Model Parameters

Our work builds on the CARAMEL modeling results of V22, (Bentz et al. 2022, hereafter B22), (Bentz et al. 2021b, hereafter B21), (Williams et al. 2020, hereafter W20), Williams et al. (2018, hereafter W18), Grier et al. (2017), hereafter G17), and Pancoast et al. (2014, hereafter P14). In this section, we provide a brief summary of the CARAMEL model detailed by P14.

Briefly, CARAMEL is a phenomenological model that uses velocity-resolved reverberation-mapping data sets to model the BLR emissivity distribution. The BLR is modeled by point particles, surrounding the black hole located at the origin, which instantaneously reemit light received from the ionizing source toward an observer.

2.1. BLR Geometry

The radial distribution of the BLR point particles is drawn from a gamma distribution with shape parameter α and scale parameter θ,

$$p(x|\alpha, \theta) \propto x^{\alpha-1}\exp\left(-\frac{x}{\theta}\right). \tag{2}$$

The distribution is then shifted from the origin by the Schwarzchild radius plus a free parameter $r_{\rm min}$, which sets the minimum BLR radius. This is then followed by a change of variables from (α, θ, $r_{\rm min}$) to (μ, β, F), such that:

$$\mu = r_{\rm min} + \alpha\theta, \tag{3}$$

$$\beta = \frac{1}{\sqrt{\alpha}}, \text{ and} \tag{4}$$

$$F = \frac{r_{\rm min}}{r_{\rm min} + \alpha\theta}. \quad (5)$$

With this change of variables, the two CARAMEL model parameters closely associated with BLR size are μ and F; the parameter μ describes the mean radius, while the parameter F describes the minimum radius in units of μ.

After the change of variables, the BLR disk thickness is then determined by the model parameter $\theta_{\rm o}$. The opening angle, $\theta_{\rm o}$, corresponds to half the angular thickness of the BLR in the angular spherical polar coordinate, such that $\theta_{\rm o} = 90^\circ$ corresponds to a spherical BLR. The BLR inclination angle, $\theta_{\rm i}$, is then determined by the angle between a face-on disk and the observer's line of sight. In this way, a face-on BLR geometry would correspond to $\theta_{\rm i} \to 0$ and an edge-on BLR geometry $\theta_{\rm i} \to 90^\circ$.

Once the BLR geometry is determined from the parameters described above and a few additional parameters (for a full description of the geometric model, please see P14), the kinematics are set by a number of parameters that allow for elliptical inflowing/outflowing orbits, and macroturbulent contributions.

2.2. BLR Kinematics

Particle velocities are modeled using both radial and tangential velocity distributions, with a fraction of particles, $f_{\rm ellip}$, on near-circular orbits around the central black hole. The remaining $1 - f_{\rm ellip}$ particles can have either inflowing or outflowing orbits, and the direction of motion is determined by the parameter $f_{\rm flow}$. Inflow motion is defined by values of $f_{\rm flow} < 0.5$ and outflow motion is defined by values of $f_{\rm flow} > 0.5$.

Whether these orbits are bound or unbound is then determined by the parameter $\theta_{\rm e}$, which describes the angle between escape velocity and circular velocity. In this way, $\theta_{\rm e} \to 0^\circ$ represents nearly unbound orbits, $\theta_{\rm e} \to 90^\circ$ represents nearly circular orbits, and values of $\theta_{\rm e} \approx 45^\circ$ represent highly elliptical (bound) orbits. Using the kinematic parameters described above, inflow/outflow motion can be summarized by the In.- Out. parameter created by W18,

$$\text{In.}-\text{Out.} = \text{sgn}(f_{\rm flow} - 0.5) \times (1 - f_{\rm ellip}) \times \cos(\theta_e), \quad (6)$$

where sgn is the sign function. Values of -1 indicate pure radial inflow and values of 1 indicate pure radial outflow.

Last, in addition to inflow/outflow motion, the model also allows for macroturbulent contributions by including the following $v_{\rm turb}$ velocity to the line-of-sight velocity:

$$v_{\rm turb} = \mathcal{N}(0, \sigma_{\rm turb})|v_{\rm circ}|, \quad (7)$$

where $|v_{\rm circ}|$ represents circular velocity as determined by the central black hole's mass, and $\mathcal{N}(0, \sigma_{\rm turb})$ is a Gaussian distribution with standard deviation $\sigma_{\rm turb}$. The free parameter $\sigma_{\rm turb}$ is allowed to range from 0.001 to 0.1 and thus represents the contribution of macroturbulent velocities. For each particle, we find the elliptical, inflowing, or outflowing velocity first, and then add the magnitude of the macroturbulent velocity, $v_{\rm turb}$, determined.

2.3. Model Results

In addition to the geometric and dynamical model parameters described above, we also include a black-hole mass parameter, $M_{\rm BH}$, with a log uniform prior between 2.78×10^4 and $1.67 \times 10^9 M_\odot$. Including black-hole mass as a model parameter allows us to constrain $M_{\rm BH}$, without the use of the scale factor, f (Equation (1)). To interpret the results, we use the posterior distribution functions CARAMEL produces for the model parameters, and report the median value and 68% confidence interval for 1σ uncertainties.

In this paper, we use the CARAMEL results found by V22 for the LAMP 2016 sample, and results from our extended sample's respective papers (P14; G17; W18; B21, and B22). We note that as outlined in the Appendix of Williams & Treu (2022), the CARAMEL code has undergone some minor modifications since its original publication. These changes were implemented for the work of V22, but not for the modeling results of the rest of the subsamples included in our extended sample: W18, G17, P14, W20, B21, and B22. However, using a subsample of AGNs modeled with the original code, we have found that the updated code used by V22 does not significantly change the results produced by the original code (e.g., W18, G17, P14, W20, B21, and B22) (L. Villafaña 2023, in preparation). For further details regarding modifications made to the code, please refer to Appendix.

3. The Virial Coefficient

A key CARAMEL result is black-hole mass, which allows us to determine an AGN-specific virial coefficient for each AGN modeled (see Equation (1)). In this section, we summarize the different ways line widths are measured for reverberation-mapping black-hole mass estimates and our methodology for determining individual AGN virial coefficients.

3.1. Line-width Measurements

The line width of the broad emission line, which is used to determine the speed of the BLR gas (Equation (1)), can either be measured from the root-mean-square (rms) spectrum, or from the mean spectrum. Measurements taken from the rms spectrum are computed with the intent that only the variable part of the line will contribute to the line-width calculation (Shen 2013). However, whenever the rms profile cannot be measured, owing to insufficient epochs or low signal-to-noise ratio, the line width is often calculated using the mean spectra instead (e.g., Denney et al. 2010).

In either case, the line width measured from the spectra selected (i.e., rms or mean) is then characterized by either the full width at half-maximum intensity (FWHM) or the line dispersion, $\sigma_{\rm line}$ (i.e., the second moment of the line). The FWHM simply corresponds to the difference between wavelengths from both sides of the peak, $P(\lambda)_{\rm max}$, at half of the height. We determine $\sigma_{\rm line}$ using the definition of Peterson et al. (2004):

$$\sigma^2_{\rm line}(\lambda) = \langle\lambda^2\rangle - \lambda_0^2, \quad (8)$$

where

$$\langle\lambda^2\rangle = \frac{\int \lambda^2 P(\lambda) d\lambda}{\int P(\lambda) d\lambda} \quad (9)$$

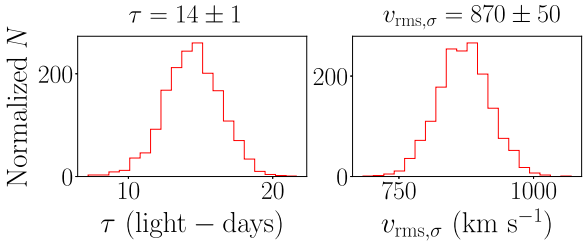

Figure 1. To propagate uncertainties, we assume Gaussian errors on the cross-correlation time-lag (left) and line-width (right) measurements given by U et al. (2022). This allows us to create distribution functions that we can utilize with our CARAMEL $M_{\rm BH}$ posterior distribution function to determine the distribution of the scale factor of an individual source, from which we use the 68% confidence interval for 1σ uncertainties.

and

$$\lambda_0 = \frac{\int \lambda P(\lambda) d\lambda}{\int P(\lambda) d\lambda}. \quad (10)$$

Both the width type (i.e., FWHM or $\sigma_{\rm line}$) and spectra (i.e., rms or mean) used to measure the line width then determine which calibrated scale factor is needed to calculate the virial $M_{\rm BH}$ (Equation (1)). For example, Woo et al. (2015) derived a constant f factor based on the M–σ_* relation calibration, for both FWHM-based and $\sigma_{\rm line}$-based $M_{\rm BH}$ estimates.

3.2. AGN-specific Virial Coefficient Calculations

For completeness, we determine all four versions of the scale factor ($\log_{10} f_{\rm FWHM,rms}$, $\log_{10} f_{\sigma,\rm rms}$, $\log_{10} f_{\rm FWHM,mean}$, and $\log_{10} f_{\sigma,\rm mean}$), although measurements using the line dispersion from the rms spectra have been suggested to produce less biased $M_{\rm BH}$ estimates (e.g., Peterson et al. 2004; Collin et al. 2006).

3.2.1. LAMP 2016 Sample

To calculate the scale factor for each LAMP 2016 source modeled by V22, we follow the same approach taken by all other previous CARAMEL works: we combine the cross-correlation time-lag ($\tau_{\rm cen}$) and line-width (v) values measured by the campaign's respective reverberation-mapping analysis (U et al. 2022) with the $M_{\rm BH}$ measurements determined from our forward-modeling approach ($M_{\rm BH}$ measurements for the LAMP 2016 sample can be found in V22).

To propagate uncertainties, we first assume Gaussian errors on the $\tau_{\rm cen}$ and v measurements using the standard deviations listed by U et al. (2022) (see Figure 1). For measurements with asymmetrical error bars, the average of the lower and upper errors is used for the standard deviation of the Gaussian distribution.

Then, we take random draws from the Gaussian distributions of the $\tau_{\rm cen}$ and v measurements, and calculate the virial product, $M_{\rm vir} = c\tau v^2/G$, until the number of draws is equal to the size of the $M_{\rm BH}$ posterior sample produced by CARAMEL. Finally, we find a posterior distribution for the scale factor by dividing the $M_{\rm BH}$ distribution produced by CARAMEL by the virial product distribution created above (see Figure 2). From the posterior distribution produced, we report the median value and use a 68% confidence interval for 1σ uncertainties. Results for the individual scale factors of the LAMP 2016 sample are listed in Table 1.

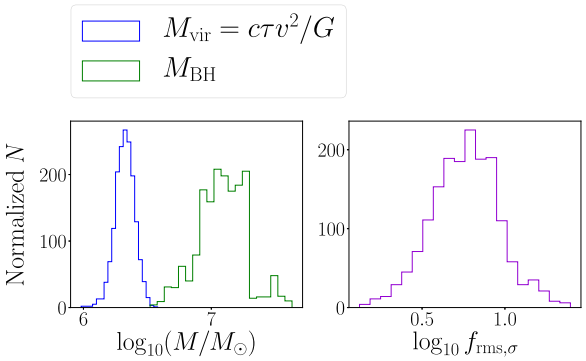

Figure 2. Taking random draws from the Gaussian distributions of the cross-correlation time lag and line widths (Figure 1), we calculate the virial product (shown in blue in the left panel) until the size of the virial product distribution is the same as that of the CARAMEL $M_{\rm BH}$ posterior distribution function (shown in green in the left panel). The logarithmic virial coefficient of any given source in our sample is found by subtracting the logarithmic virial product distribution from the logarithmic CARAMEL $M_{\rm BH}$ posterior distribution (i.e., dividing the original, nonlogarithmic distributions). The resulting distribution of logarithmic scale factor ($\log_{10}(f_{\rm rms,\sigma})$) is shown on the right panel, which allows us to report errors on our measurement by quoting the 68% confidence interval as define by the distribution.

3.2.2. Extended Sample

We extend our sample (see Table 2) by combining our results with prior CARAMEL studies, namely, seven from LAMP 2011 (W18), four from AGN10 (G17), five from LAMP 2008 (P14), one from AGNSTORM (W20), one from B21, and one from B22.

The line widths used to compute the virial coefficient using the approach described above can be found in Table 3. All line widths correspond to those used in our previous CARAMEL studies, with the exception of the four from the AGN10 (G17) campaign. The line widths previously used did not have the narrow-line component removed. In order to remain consistent within our extended sample when searching for correlations with line-profile shape, we remeasured the line widths of these four points using the data from G17, in which the narrow-line contribution had been removed. To remeasure these line widths, we used the methods of U et al. (2022) and computed a Monte Carlo bootstrapping procedure for error analysis.

The values of the individual AGN-specific virial coefficients are also found in their respective CARAMEL papers and were determined in the same fashion as the LAMP 2016 sample described above.

4. Results

Using the individual AGN-specific virial coefficients determined for our extended sample, and enabled by our CARAMEL forward-modeling approach, we carry out a systematic investigation of correlations between f and observables.

We use the IDL routine `linmix_err` (Kelly 2007) to perform a Bayesian linear regression in order to account for correlated measurement uncertainties. Doing so allows us to analyze the actual intrinsic correlation of any two parameters without worrying about a false increase due to correlated measurement uncertainties. This is especially important for our search for correlations with scale factor since individual scale factors are determined using our model $M_{\rm BH}$ measurements, and therefore uncertainties in the scale factor are connected to uncertainties in other model parameters.

Table 1
Inferred Scale Factors

Galaxy	$\log_{10}(f_{\mathrm{rms},\sigma})$	$\log_{10}(f_{\mathrm{rms,FWHM}})$	$\log_{10}(f_{\mathrm{mean},\sigma})$	$\log_{10}(f_{\mathrm{mean,FWHM}})$
PG 2209+184	$0.84^{+0.21}_{-0.20}$	$0.08^{+0.21}_{-0.20}$	$0.71^{+0.21}_{-0.19}$	$-0.11^{+0.21}_{-0.20}$
MCG +04-22-042	$1.21^{+0.41}_{-0.31}$	$0.54^{+0.41}_{-0.31}$	$1.08^{+0.41}_{-0.31}$	$0.34^{+0.41}_{-0.31}$
Mrk 1392	$1.10^{+0.12}_{-0.14}$	$0.32^{+0.13}_{-0.14}$	$1.02^{+0.12}_{-0.14}$	$0.19^{+0.12}_{-0.14}$
RBS 1303	$0.05^{+0.27}_{-0.20}$	$-0.23^{+0.25}_{-0.17}$	$0.07^{+0.24}_{-0.16}$	$-0.46^{+0.23}_{-0.16}$
RBS 1917	$0.82^{+0.32}_{-0.34}$	$0.54^{+0.26}_{-0.32}$	$0.54^{+0.27}_{-0.32}$	$-0.08^{+0.50}_{0.32}$
Mrk 841	$0.62^{+0.50}_{-0.34}$	$-0.40^{+0.47}_{-0.38}$	$0.67^{+0.50}_{-0.36}$	$-0.38^{+0.50}_{-0.36}$
RXJ 2044.0+2833	$0.76^{+0.19}_{-0.19}$	$0.02^{+0.18}_{-0.20}$	$0.66^{+0.18}_{-0.20}$	$-0.04^{+0.18}_{-0.20}$
NPM1G+27.0587	$0.98^{+0.51}_{-0.47}$	$0.53^{+0.52}_{-0.46}$	$1.01^{+0.50}_{-0.47}$	$0.37^{+0.52}_{-0.46}$
Mrk 1048	$1.05^{+0.65}_{-0.57}$	$0.33^{+0.64}_{-0.61}$	$1.00^{+0.66}_{-0.57}$	$0.16^{+0.66}_{-0.58}$

Note. Individual scale factors for the nine LAMP 2016 sources modeled by V22. Values were determined using our model M_{BH} estimates and corresponding line widths and cross-correlation time lags found by U et al. (2022). Individual scale factors of our extended sample can be found in their respective CARAMEL papers: P14; G17; W18; W20; B21; and B22.

Table 2
Extended Sample

Campaign	Galaxy	Redshift	$\log_{10}(M_{\mathrm{BH}}/M_{\odot})$
Lick AGN Monitoring Project (LAMP 2008; Pancoast et al. 2014, hereafter P14)			
	Arp 151	0.02109	$6.62^{+0.10}_{-0.13}$
	Mrk 1310	0.01941	$7.42^{+0.26}_{-0.27}$
	NGC 5548	0.01718	$7.51^{+0.23}_{-0.14}$
	NGC 6814	0.00521	$6.42^{+0.24}_{-0.18}$
	SBS 1116+583A	0.02787	$6.99^{+0.32}_{-0.25}$
2010 AGN monitoring campaign at MDM Observatory (AGN10; Grier et al. 2017, hereafter G17)	Mrk 335	0.0258	$7.25^{+0.10}_{-0.10}$
	Mrk 1501	0.0893	$7.86^{+0.20}_{-0.17}$
	3C 120	0.0330	$7.84^{+0.14}_{-0.19}$
	PG 2130+099	0.0630	$6.92^{+0.24}_{-0.23}$
Lick AGN Monitoring Project (LAMP 2011; Williams et al. 2018, hereafter W18)	Mrk 50	0.0234	$7.50^{+0.25}_{-0.18}$
	Mrk 141	0.0417	$7.46^{+0.15}_{-0.21}$
	Mrk 279	0.0305	$7.58^{+0.08}_{-0.08}$
	Mrk 1511	0.0339	$7.11^{+0.20}_{-0.17}$
	NGC 4593	0.0090	$6.65^{+0.27}_{-0.15}$
	Zw 229-015	0.0279	$6.94^{+0.14}_{-0.14}$
	PG 1310-108	0.0343	$6.48^{+0.21}_{-0.18}$
Space Telescope and Optical Reverberation Mapping Project (AGNSTORM; Williams et al. 2020, hereafter W20)			
	NGC 5548	0.017175	$7.64^{+0.21}_{-0.18}$
AGN monitoring campaign at Las Cumbres Observatory (LCO; Bentz et al. 2021b, hereafter B21)			
	NGC 3783	0.097	$7.51^{+0.26}_{-0.13}$
Lick AGN Monitoring Project (LAMP 2016; Villafaña et al. 2022, hereafter V22)	PG 2209+184	0.07000	$7.53^{+0.19}_{-0.20}$
	RBS 1917	0.06600	$7.04^{+0.23}_{-0.35}$
	MCG +04-22-042	0.03235	$7.59^{+0.42}_{-0.28}$
	NPM1G +27.0587	0.06200	$7.64^{+0.40}_{-0.36}$
	Mrk 1392	0.03614	$8.16^{+0.11}_{-0.13}$
	RBS 1303	0.04179	$6.79^{+0.19}_{-0.11}$
	Mrk 1048	0.04314	$7.79^{+0.44}_{-0.48}$
	RXJ 2044.0+2833	0.05000	$7.09^{+0.17}_{-0.17}$
	Mrk 841	0.03642	$7.62^{+0.50}_{-0.30}$
AGN monitoring campaign at MDM Observatory (MDM; Bentz et al. 2022, hereafter B22)			
	NGC 4151	0.0033	$7.22^{+0.11}_{-0.10}$

Note. Extended sample includes sources modeled by P14, G17, W18, W20, B21, and B22, in addition to the most recent sampled modeled by V22. Column 1 specifies the campaign from which data were collected and galaxy name is found in column 2. Columns 3 and 4 list the galaxy's redshift and CARAMEL M_{BH} estimate, as defined by the 68% confidence interval of the resultant posterior distribution function, respectively.

Table 3
Line Widths and Line-profile Shapes of Extended Sample

Galaxy	rms			Mean		
	FWHM	$\sigma_{\rm line}$	$\log_{10}({\rm FWHM}/\sigma)$	FWHM	$\sigma_{\rm line}$	$\log_{10}({\rm FWHM}/\sigma)$
Arp 151 (P11)	2458 ± 82[a]	1295 ± 37[a]	0.28 ± 0.02	3076 ± 39[a]	1726 ± 17[a]	0.25 ± 0.007
Mrk 1310 (P11)	1823 ± 157[a]	921 ± 135[a]	0.30 ± 0.07	2425 ± 19[a]	1229 ± 12[a]	0.29 ± 0.005
NGC 5548 (P11)	$12{,}539 \pm 1927$[a]	3900 ± 266[a]	$0.51^{+0.08}_{-0.07}$	$12{,}402 \pm 111$[a]	4354 ± 25[a]	0.45 ± 0.004
NGC 6814 (P11)	2945 ± 283[a]	1697 ± 224[a]	0.24 ± 0.07	3129 ± 14[a]	1744 ± 12[a]	0.25 ± 0.003
SBS 1116+583A (P11)	…	…	…	3135 ± 36[a]	1460 ± 23[a]	0.33 ± 0.01
Mrk 335 (G17)	1853 ± 79[b]	1239 ± 78[b]	0.17 ± 0.03	2018 ± 1[b]	1354 ± 34[b]	0.17 ± 0.01
Mrk 1501 (G17)	3476 ± 214[b]	1401 ± 48[b]	0.40 ± 0.03	3780 ± 25[b]	1486 ± 48[b]	0.41 ± 0.01
3C 120 (G17)	2035 ± 97[b]	1218 ± 47[b]	0.22 ± 0.03	2893 ± 22[b]	1175 ± 26[b]	0.39 ± 0.01
PG 2130+099 (G17)	1409 ± 143[b]	1459 ± 93[b]	-0.02 ± 0.05	2107 ± 32[b]	1321 ± 11[b]	0.20 ± 0.01
Mrk 50 (W18)	3355 ± 128[c]	2020 ± 103[c]	0.22 ± 0.03	4101 ± 56[c]	2024 ± 31[c]	0.31 ± 0.01
Mrk 141 (W18)	…	…	…	5129 ± 45[c]	2280 ± 21[c]	0.35 ± 0.01
Mrk 279 (W18)	3306 ± 338[c]	1778 ± 71[c]	0.27 ± 0.05	4099 ± 43[c]	1821 ± 13[c]	0.35 ± 0.01
Mrk 1511 (W18)	3236 ± 65[c]	1506 ± 42[c]	$0.33^{+0.02}_{-0.01}$	4154 ± 28[c]	1828 ± 12[c]	0.36 ± 0.004
NGC 4593 (W18)	3597 ± 72[c]	1601 ± 40[c]	0.35 ± 0.01	4264 ± 41[c]	1925 ± 38[c]	0.35 ± 0.01
Zw 229-015 (W18)	1789 ± 93[c]	1609 ± 109[c]	0.05 ± 0.04	3705 ± 203[c]	1747 ± 56[c]	0.33 ± 0.03
PG 1310-108 (W18)	…	…	…	3422 ± 21[c]	1823 ± 20[c]	0.27 ± 0.01
NGC 5548 (W20)	$10{,}861 \pm 739$[d]	4115 ± 513[d]	$0.42^{+0.06}_{-0.07}$	9612 ± 427[d]	3983 ± 150[d]	$0.38^{+0.02}_{-0.03}$
NGC 3783 (B21)	4278 ± 676[e]	1619 ± 137[e]	$0.42^{+0.08}_{-0.07}$	4486 ± 35[e]	1825 ± 19[e]	0.39 ± 0.01
PG 2209+184 (V22)	3247 ± 88[f]	1353 ± 64[f]	0.38 ± 0.02	4045 ± 34[f]	1573 ± 40[f]	0.41 ± 0.01
MCG +04-22-042 (V22)	2120 ± 39[f]	977 ± 29[f]	$0.34^{+0.01}_{-0.02}$	2658 ± 57[f]	1141 ± 39[f]	0.37 ± 0.02
Mrk 1392 (V22)	3690 ± 138[f]	1501 ± 38[f]	0.39 ± 0.02	4267 ± 25[f]	1635 ± 13[f]	0.417 ± 0.004
RBS 1303 (V22)	1738 ± 113[f]	1292 ± 156[f]	0.13 ± 0.06	2286 ± 21[f]	1243 ± 26[f]	0.26 ± 0.01
RBS 1917 (V22)	1653 ± 287[f]	851 ± 154[f]	$0.14^{+0.07}_{-0.09}$	2399 ± 11[f]	1180 ± 50[f]	0.31 ± 0.02
Mrk 841 (V22)	7452 ± 660[f]	2278 ± 96[f]	0.51 ± 0.04	7073 ± 311[f]	2139 ± 55[f]	0.52 ± 0.02
RXJ 2044.0+2833 (V22)	2047 ± 72[f]	870 ± 50[f]	0.37 ± 0.03	2196 ± 31[f]	989 ± 32[f]	$0.35^{+0.01}_{-0.02}$
NPM1G+27.0587 (V22)	2893 ± 177[f]	1735 ± 136[f]	$0.22^{+0.04}_{-0.05}$	3501 ± 28[f]	1683 ± 42[f]	0.32 ± 0.01
Mrk 1048 (V22)	4042 ± 406[f]	1726 ± 76[f]	0.37 ± 0.05	4830 ± 80[f]	1840 ± 58[f]	0.42 ± 0.02
NGC 4151 (B22)	4711 ± 750[g]	2680 ± 64[g]	$0.25^{+0.08}_{-0.06}$	7382 ± 279[g]	2724 ± 17[g]	0.43 ± 0.02

Notes. All line widths are given in km s^{-1}. A line-profile shape of $\log_{10}({\rm FWHM}/\sigma) = 0.371$ corresponds to a Gaussian profile, while $\log_{10}({\rm FWHM}/\sigma) < 0.371$ corresponds to a Lorentz profile, and $\log_{10}({\rm FWHM}/\sigma) > 0.371$ corresponds to a flat-topped profile. References for line widths are as follows.
[a] Park et al. (2012b).
[b] This work, the measurements used in previous CARAMEL studies originated from Grier et al. (2012), which did not remove the narrow-line contribution. Thus, we remeasured using the data and spectral decompositions used by G17, in order to ensure these line-width measurements were consistent with the rest of the sample, i.e., with the narrow-line contribution removed.
[c] Barth et al. (2015).
[d] Pei et al. (2017).
[e] Bentz et al. (2021a).
[f] U et al. (2022).
[g] Bentz et al. (2006).

To quantify the strength of any correlation, we compare the median fit slope to the 1σ uncertainty in the slope and determine our level of confidence using the following intervals we have defined in our previous study W18: we classify 0–2σ as no evidence, 2–3σ as marginal evidence, 3–5σ as evidence, and $>5\sigma$ as conclusive evidence.

Overall, we find the following correlations with at least marginal evidence as defined by our confidence intervals:

1. Black-hole Mass:

$\log_{10}(f_{{\rm mean},\sigma})$ versus $\log_{10}(M_{\rm BH}/M_\odot)$;
$\beta = 0.51 \pm 0.15$, $\sigma_{\rm int} = 0.22 \pm 0.05$,
3.4σ evidence

$\log_{10}(f_{{\rm rms},\sigma})$ versus $\log_{10}(M_{\rm BH}/M_\odot)$
$\beta = 0.47 \pm 0.17$, $\sigma_{\rm int} = 0.25^{+0.06}_{-0.05}$,
2.8σ marginal evidence

2. Opening Angle (BLR disk thickness):

$\log_{10}(f_{\rm mean,FWHM})$ versus θ_o;
$\beta = -0.96^{+0.47}_{-0.43}$, $\sigma_{\rm int} = 0.22^{+0.06}_{-0.05}$
2.1σ marginal evidence

$\log_{10}(f_{\rm rms,FWHM})$ versus θ_o;
$\beta = -1.15^{+0.48}_{-0.46}$, $\sigma_{\rm int} = 0.21^{+0.06}_{-0.05}$
2.4σ marginal evidence

3. Inclination Angle:

$\log_{10}(f_{\rm mean,FWHM})$ versus θ_i;
$\beta = -1.45^{+0.53}_{-0.56}$, $\sigma_{\rm int} = 0.17^{+0.05}_{-0.04}$
2.6σ marginal evidence

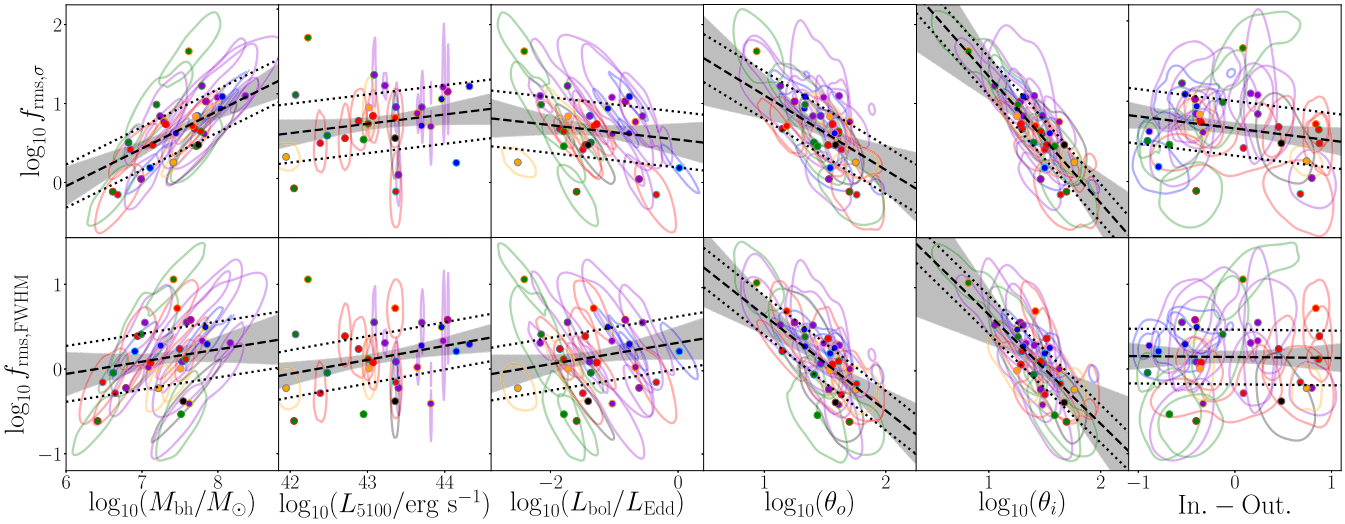

Figure 3. Correlations between the scale factor $\log_{10} f_{\mathrm{rms},\sigma}$ (top) and $\log_{10} f_{\mathrm{rms,FWHM}}$ (bottom) with select AGNs and model parameters. From left to right: M_{BH}, optical luminosity, Eddington ratio, Hβ -emitting BLR opening angle (disk thickness), Hβ -emitting BLR inclination angle, and our "inflow–outflow" parameter. The colored dots and contours show the median and 68% confidence regions of the 2D posterior PDFs for each AGN. The dashed black lines and gray-shaded regions give the median and 68% confidence intervals of the linear regression. Dotted lines are offset above and below the dashed line by the median value of the intrinsic scatter. Purple points are for the AGNs from V22, red points are from W18, green points are from P14, blue points are from G17, the black point is from W20, and the orange points are from B21 and B22.

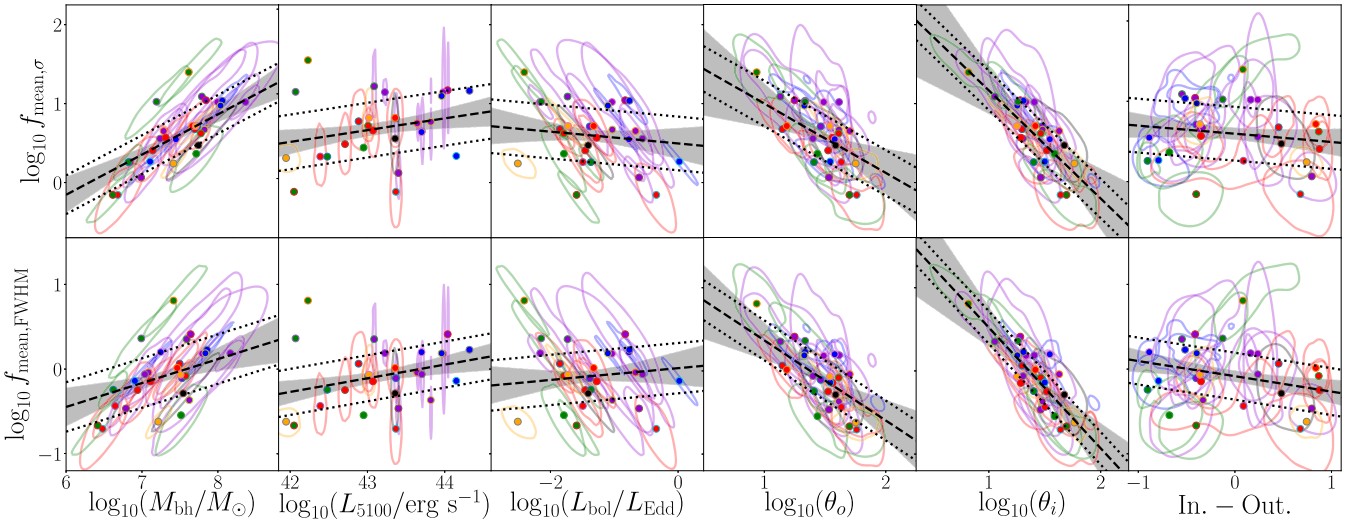

Figure 4. Correlations between the scale factor $\log_{10} f_{\mathrm{mean},\sigma}$ (top) and $\log_{10} f_{\mathrm{mean,FWHM}}$ (bottom) with select AGNs and model parameters. From left to right: M_{BH}, optical luminosity, Eddington ratio, Hβ -emitting BLR opening angle (disk thickness), Hβ -emitting BLR inclination angle, and our "inflow–outflow" parameter. The colored dots and contours show the median and 68% confidence regions of the 2D posterior PDFs for each AGN. The dashed black lines and gray-shaded regions give the median and 68% confidence intervals of the linear regression. Dotted lines are offset above and below the dashed line by the median value of the intrinsic scatter. Purple points are for the AGNs from V22, red points are from W18, green points are from P14, blue points are from G17, the black point is from W20, and the orange points are from B21 and B22.

Table 4
Linear Regression Results for rms Spectrum Scale Factors

f type		$\log_{10}(M_{\mathrm{BH}}/M_{\odot})$	$\log_{10}(L_{5100}/\mathrm{erg\ s^{-1}})$	$\log_{10}(L_{\mathrm{bol}}/L_{\mathrm{Edd}})$	θ_o (deg.)	θ_i (deg.)	In. − Out. param.
rms, σ	α	$-2.74^{+1.22}_{-1.24}$	$-4.03^{+5.19}_{-5.03}$	0.55 ± 0.21	$2.05^{+0.81}_{-0.90}$	$2.95^{+0.97}_{-0.96}$	0.67 ± 0.08
	β	0.47 ± 0.17	0.11 ± 0.12	$-0.09^{+0.14}_{-0.15}$	$-0.95^{+0.60}_{-0.54}$	$-1.61^{+0.66}_{-0.68}$	-0.16 ± 0.14
	σ_{int}	$0.25^{+0.06}_{-0.05}$	$0.31^{+0.09}_{-0.08}$	$0.32^{+0.08}_{-0.07}$	$0.28^{+0.07}_{-0.05}$	$0.22^{+0.06}_{-0.05}$	$0.31^{+0.08}_{-0.07}$
rms, FWHM	α	$-0.91^{+1.41}_{-1.43}$	$-7.18^{+4.70}_{-4.33}$	$0.32^{+0.19}_{-0.20}$	$1.82^{+0.68}_{-0.71}$	$1.99^{+0.99}_{-1.16}$	0.15 ± 0.07
	β	$0.14^{+0.20}_{-0.19}$	$0.17^{+0.10}_{-0.11}$	$0.13^{+0.13}_{-0.14}$	$-1.15^{+0.48}_{-0.46}$	$-1.31^{+0.80}_{-0.69}$	-0.01 ± 0.14
	σ_{int}	$0.29^{+0.08}_{-0.07}$	0.24 ± 0.09	$0.27^{+0.09}_{-0.08}$	$0.21^{+0.06}_{-0.05}$	$0.20^{+0.06}_{-0.05}$	$0.29^{+0.09}_{-0.08}$

Note. Linear regression results used to determine correlations between the scale factor f and select AGNs and model parameters shown in Figure 3. The parameters α and β represent the constant and slope of the linear regression, respectively. While σ_{int} represents the standard deviation of the intrinsic scatter. The corresponding relationship is therefore given by $\log_{10} f = \alpha + \beta \times$ parameter $+ \mathcal{N}(0, \sigma_{\mathrm{int}})$.

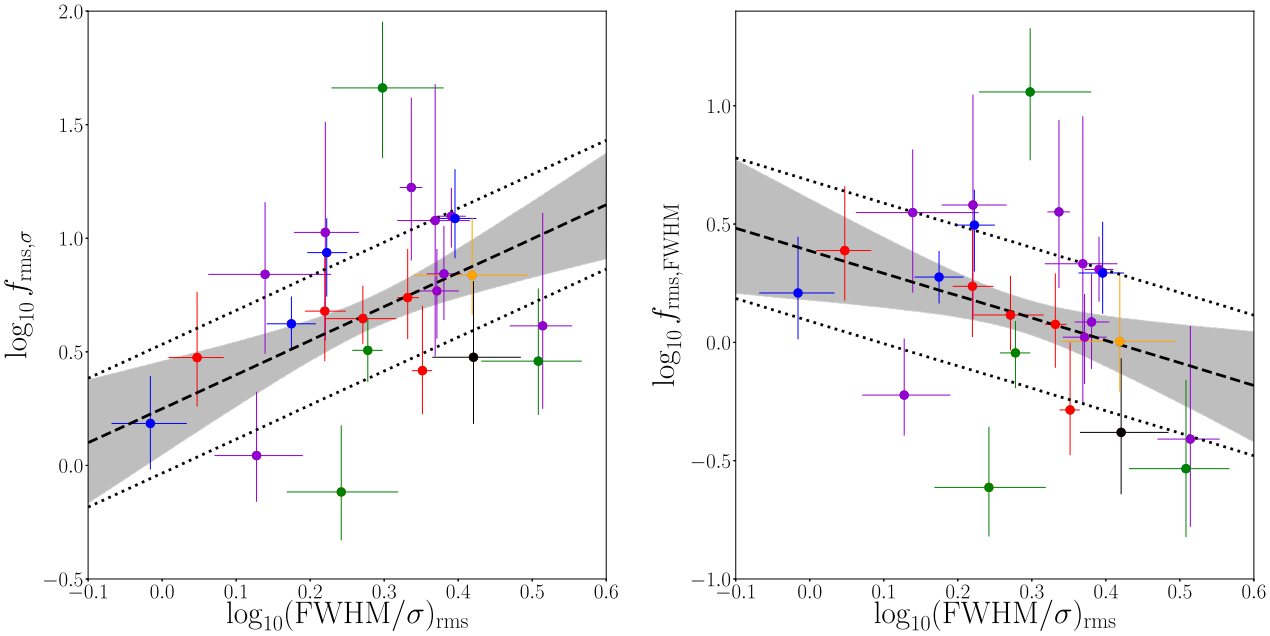

Figure 5. Correlations between rms line-profile shape and scale factor determined using line dispersion (left) and FWHM (right). The dashed black lines and gray-shaded regions give the median and 68% confidence intervals of the linear regression. Dotted lines are offset above and below the dashed ine by the median value of the intrinsic scatter. Purple points are for the AGNs from V22, red points are from W18, green points are from P14, blue points are from G17, the black point is from W20, and the two orange points are from B21 and B22.

Table 5
Linear Regression Results for Mean Spectrum Scale Factors

f type		$\log_{10}(M_{\mathrm{BH}}/M_{\odot})$	$\log_{10}(L_{5100}/\mathrm{erg\ s^{-1}})$	$\log_{10}(L_{\mathrm{bol}}/L_{\mathrm{Edd}})$	θ_o (deg.)	θ_i (deg.)	In. − Out. param.
mean, σ	α	$-3.11^{+1.06}_{-1.10}$	$-5.47^{+4.87}_{-4.61}$	$0.51^{+0.19}_{-0.20}$	$1.88^{+0.75}_{-0.88}$	$2.53^{+0.98}_{-0.94}$	0.60 ± 0.08
	β	0.51 ± 0.15	0.14 ± 0.11	$-0.07^{+0.13}_{-0.14}$	$-0.88^{+0.59}_{-0.50}$	$-1.37^{+0.66}_{-0.68}$	-0.10 ± 0.14
	σ_{int}	0.22 ± 0.05	$0.29^{+0.08}_{-0.07}$	$0.30^{+0.08}_{-0.06}$	$0.26^{+0.06}_{-0.05}$	0.23 ± 0.05	$0.30^{+0.08}_{-0.07}$
mean, FWHM	α	$-1.99^{+1.26}_{-1.28}$	$-7.13^{+4.37}_{-4.04}$	0.01 ± 0.20	$1.33^{+0.63}_{-0.70}$	$1.97^{+0.81}_{-0.75}$	-0.08 ± 0.07
	β	$0.26^{+0.18}_{-0.17}$	$0.16^{+0.09}_{-0.10}$	$0.07^{+0.13}_{-0.14}$	$-0.96^{+0.47}_{-0.43}$	$-1.45^{+0.53}_{-0.56}$	-0.18 ± 0.12
	σ_{int}	0.26 ± 0.06	$0.23^{+0.08}_{-0.07}$	$0.26^{+0.08}_{-0.07}$	$0.22^{+0.06}_{-0.05}$	$0.17^{+0.05}_{-0.04}$	$0.24^{+0.07}_{-0.06}$

Note. Linear regression results used to determine correlations between the scale factor f and select AGNs and model parameters shown in Figure 4. The parameters α and β represent the constant and slope of the linear regression, respectively. While σ_{int} represents the standard deviation of the intrinsic scatter. The corresponding relationship is therefore given by $\log_{10} f = \alpha + \beta \times$ parameter $+ \mathcal{N}(0, \sigma_{\mathrm{int}})$.

$\log_{10}(f_{\mathrm{rms},\sigma})$ versus θ_i;
$\beta = -1.61^{+0.66}_{-0.68}$, $\sigma_{\mathrm{int}} = 0.22^{+0.06}_{-0.05}$
2.4σ marginal evidence

$\log_{10}(f_{\mathrm{mean},\sigma})$ versus θ_i;
$\beta = -1.37^{+0.66}_{-0.68}$, $\sigma_{\mathrm{int}} = 0.23 \pm 0.05$
2.0σ marginal evidence

4. Line-profile Shape:

$(\mathrm{FWHM}/\sigma)_{\mathrm{rms}}$ versus $\log_{10}(f_{\mathrm{rms},\sigma})$;
$\beta = 1.50^{+0.67}_{-0.71}$, $\sigma_{\mathrm{int}} = 0.24^{+0.09}_{-0.08}$
2.2σ marginal evidence

4.1. Correlations between f and AGN/BLR Parameters

In an effort to uncover any regularities in the behavior of the BLR and gain a better understanding of the inner regions of AGNs, we investigate correlations between scale factor and AGN/BLR parameters determined by our forward-modeling approach. Overall, we find similar trends for both the rms and mean spectrum; see Figures 3 and 4 (respectively), and Tables 4 and 5, for their corresponding regression values. We reiterate that covariance between variables is taken into account in our analysis, in order to avoid spurious correlations.

We find evidence (3.4σ) for a correlation between scale factor and M_{BH} when using the mean spectrum and line dispersion line width, i.e., $\log_{10}(f_{\mathrm{mean},\sigma})$ ($\beta = 0.51 \pm 0.15$), which had not been previously found by P14, G17, or W18. Similarly, we find marginal evidence (2.8σ) for a correlation between $\log_{10}(f_{\mathrm{rms},\sigma})$ and M_{BH} ($\beta = 0.47 \pm 0.17$). This correlation suggests that the BLR geometry and dynamics may be correlated with M_{BH}.

We also find marginal evidence for an anticorrelation with BLR opening angle, θ_o, which is the CARAMEL model parameter that represents the BLR disk thickness, when using FWHM line-width measurements with both the mean ($\beta = -0.96^{+0.47}_{-0.43}$) and rms ($\beta = -1.15^{+0.48}_{-0.46}$) spectrum. Such a

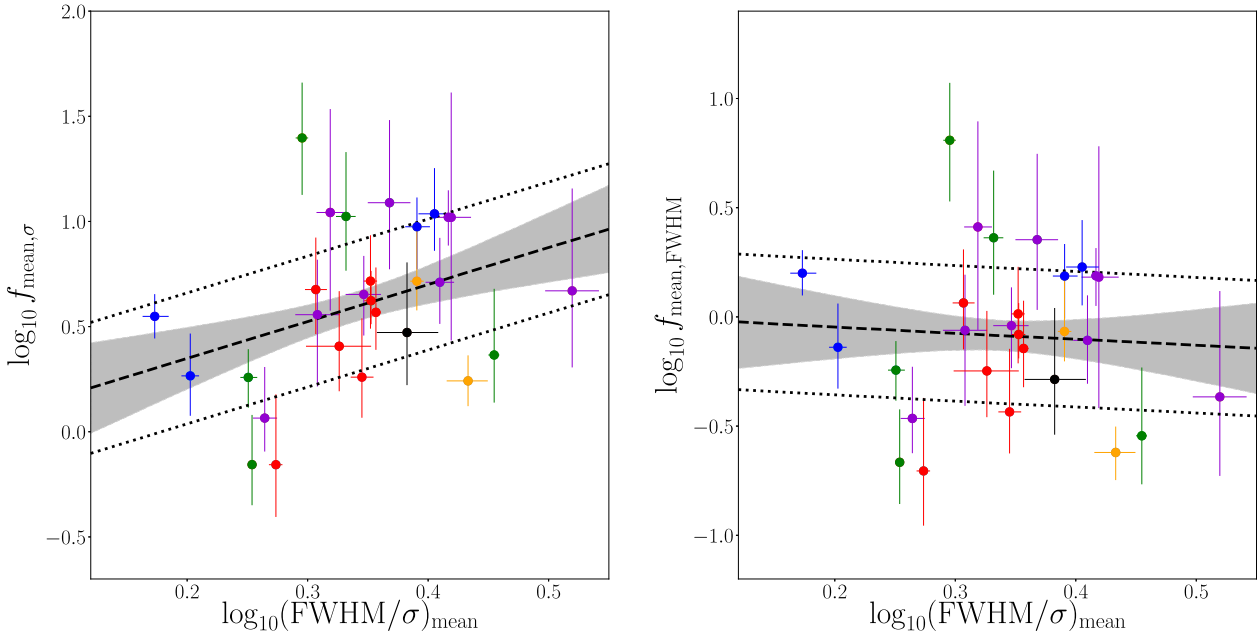

Figure 6. Correlations between mean line-profile shape and scale factor determined using line dispersion (left) and FWHM (right). The dashed black lines and gray-shaded regions give the median and 68% confidence intervals of the linear regression. Dotted lines are offset above and below the dashed line by the median value of the intrinsic scatter. Purple points are for the AGNs from V22, red points are from W18, green points are from P14, blue points are from G17, the black point is from W20, and the two orange points are from B21 and B22.

Table 6
Linear Regression Results for Line-profile Shape vs. Scale Factor

Line-profile Shape		$\log_{10} f_{\sigma}$	$\log_{10} f_{\mathrm{FWHM}}$
$\log_{10}\left(\frac{\mathrm{FWHM}}{\sigma}\right)_{\mathrm{mean}}$	α	-0.001 ± 0.32	$0.01^{+0.31}_{-0.32}$
	β	$1.76^{+0.94}_{-0.93}$	$-0.28^{+0.93}_{-0.92}$
	σ_{int}	$0.28^{+0.08}_{-0.06}$	$0.28^{+0.08}_{-0.06}$
$\log_{10}\left(\frac{\mathrm{FWHM}}{\sigma}\right)_{\mathrm{rms}}$	α	$0.25^{+0.21}_{-0.20}$	$0.39^{+0.22}_{-0.21}$
	β	$1.50^{+0.67}_{-0.71}$	$-0.95^{+0.69}_{-0.73}$
	σ_{int}	$0.24^{+0.09}_{-0.08}$	$0.26^{+0.09}_{-0.07}$

Note. Linear regression results for line-profile shape versus scale factor. The parameters α and β represent the constant and slope of the regression, respectively, while σ_{int} represents the standard deviation of the intrinsic scatter. The corresponding relationship is therefore given by $\log_{10}(f) = \alpha + \beta \log_{10}(\mathrm{FWHM}/\sigma) + \mathcal{N}(0, \sigma_{\mathrm{int}})$.

correlation with BLR disk thickness had also not been previously found in any previous CARAMEL studies.

Finally, in agreement with previous results (P14; G17; W18), we find marginal evidence for an anticorrelation with BLR inclination angle and the virial coefficient, as measured when using the σ line width with both the rms ($\beta = -1.61^{+0.66}_{-0.68}$) and mean ($\beta = -1.37^{+0.67}_{-0.71}$) spectra. Additionally, we also find marginal evidence for an anticorrelation when using the FWHM line width and the mean spectrum ($\beta = -1.45^{+0.53}_{-0.56}$). This correlation was predicted by both Collin et al. (2006) and Goad et al. (2012), and is expected for a disk-like BLR because an increase in BLR inclination angle would result in an increased observed line-of-sight velocity and therefore increased line-width measurement. Hence, in order to recover the same M_{BH}, a smaller scale factor would be required, producing an anticorrelation like the one that is apparent in our work.

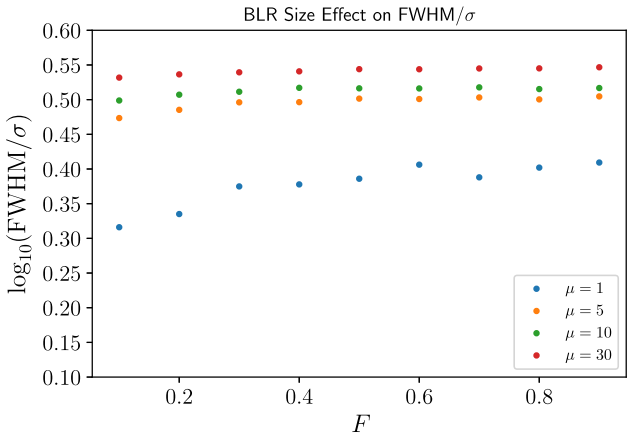

Figure 7. We investigate the role of BLR radius in line-profile shape using CARAMEL models by varying the parameters μ and F, and holding all other model parameters constant. As described in the text, the parameter μ defines the mean BLR radius and the parameter F defines the minimum radius in units of μ. Different mean BLR radii, μ, are depicted in different colors: 1 light-day is shown in blue, 5 light-days is shown in orange, 10 light-days is shown in green, and 30 light-days is shown in red. As expected, smaller values of $\log_{10}(\mathrm{FWHM}/\sigma)_{\mathrm{mean}}$ on the y-axis, are seen with decreasing μ. Additionally, within the four different mean radii, μ, a slight decrease is seen for a decrease in minimum radius, as depicted by decreasing values of F shown on the x-axis.

Before proceeding, it is important to note that although the correlations we have discovered with opening angle (BLR disk thickness) and inclination angle fall under our definition of marginally significant, they lack any real utility as BLR disk thickness is not an observable or a measurable quantity and inclination-angle measurements using radio jets (e.g., Jorstad et al. 2005; Agudo et al. 2012) are not possible for all cases. For these reasons, we now explore the existence of correlations between scale factor and a direct observable line-profile shape, that is, the ratio of the FWHM to the dispersion σ_{line}, as such a

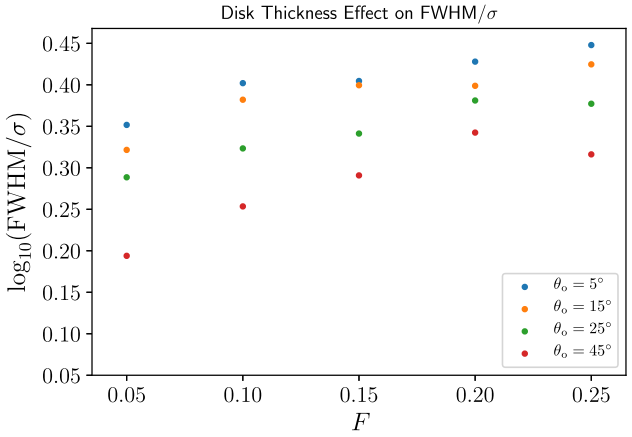

Figure 8. We investigate the role of BLR disk thickness in line-profile shape using CARAMEL toy models by varying the parameter θ_o and minimum radius F, while holding all other model parameters constant. A mean radius of $\mu = 1$ light-day is used, while minimum radius as defined by F is varied using values $F = 0$–0.3, as depicted by the x-axis. Different BLR disk thickness/opening angles, θ_o, are depicted in different colors: $\theta_o = 5°$ is shown in blue, $\theta_o = 15°$ is shown in orange, $\theta_o = 25°$ is shown in green, $\theta_o = 45°$ is shown in red. An opening angle of $\theta_o = 45°$, shown in red, corresponds to a spherical structure and produces broad lines with smaller values of $\log_{10}(\mathrm{FWHM}/\sigma)_{\mathrm{mean}}$, as expected.

correlation would provide an observational proxy for the virial coefficient and thus a more reliable way to calibrate f.

4.2. Line-profile Shape as an Observational Proxy

We search for correlations with scale factor and line-profile shape using both the rms and mean spectrum (see Figures 5 and 6, respectively), where we have used only the shape of the Hβ broad emission line by itself (i.e., we have isolated the broad emission from the narrow emission component). Line widths and line-profile shapes used for our extended sample are listed in Table 3.

We find marginal evidence (2.2σ) for a correlation between $\log_{10}(f_{\mathrm{rms},\sigma})$ and line-profile shape, when using the rms spectrum ($\beta = 1.50^{+0.67}_{-0.71}$). When using the mean spectrum, however, the correlation falls short of being considered marginal evidence and is quantified by 1.9σ (see the left-most panels of Figures 5 and 6, respectively). We do not find any evidence for a correlation with the virial coefficient when a FWHM line width is used, in either the rms or mean spectrum (see the right-most panels of Figures 5 and 6).

Although stronger evidence is needed to recommend the widespread use of this relationship, this result is promising; further investigations with increased sample size in our dynamic modeling may help elucidate the correlation we have found.

5. The Role of BLR Geometry and Kinematics on Line-profile Shape

From the correlations found in our work, we focus on the correlation found with $\log_{10}(\mathrm{FWHM}/\sigma)$, which has significant potential to improve the way the virial coefficient is calibrated. The relationship has an intrinsic scatter of similar magnitude to that of the local M_{BH}–σ_* relation (see Table 6), which suggests another intrinsic relation of AGNs, and further validates the idea of using the line-profile shape of broad emission lines as a tracer for the inner regions of AGNs (Collin et al. 2006). In an attempt to gain a better understanding, we employ CARAMEL models to test how BLR geometry and kinematics affects line-profile shape.

In particular, we aim to understand the line profiles with $\log_{10}(\mathrm{FWHM}/\sigma)_{\mathrm{mean}} \approx 0.1$–$0.2$. While line profiles with $\log_{10}(\mathrm{FWHM}/\sigma) = 0.37$ are best described by a Gaussian and are due to rotational Doppler broadening, Lorentz profiles (e.g., $\log_{10}(\mathrm{FWHM}/\sigma) < 0.37$) are thought to be a result of turbulent and/or inflow/outflow motions (Kollatschny & Zetzl 2013). In the following subsections, we investigate the effect of BLR size, disk thickness, inflow/outflow motion, and turbulent motion on Hβ broad-line-profile shapes.

5.1. BLR Size

We begin by testing the effect of BLR size, since the extended wings in a Lorentz profile are due to high-velocity gas near the black hole. Thus, assuming Keplerian orbits, we expect narrower line-profile shapes to correspond to smaller BLR radii. We manipulate the CARAMEL model parameters associated with BLR radius, μ and F, while keeping all other parameters constant. The values chosen for other relevant geometry and kinematics are as follows: $\theta_i = 20°$, $\theta_o = 20°$, $\beta = 1.0$, $\log_{10}(M_{\mathrm{BH}}/M_\odot) = 7.5$, $f_{\mathrm{flow}} = 0.5$, $f_{\mathrm{ellip}} = 1.0$, $\theta_e = 90°$, $\sigma_{\mathrm{turb}} = 0.001$. We choose the parameters to reflect particles with bound circular orbits (no inflow/outflow motion) and minimal contribution from macroturbulent velocities.

As shown in Figure 7, we find that a smaller BLR size produces a smaller value of $\log_{10}(\mathrm{FWHM}/\sigma)$, as expected. However, we do not find any line-profile shapes in the region of special interest, $\log_{10}(\mathrm{FWHM}/\sigma)_{\mathrm{mean}} \approx 0.1$–$0.2$, which suggests that bound circular orbits cannot produce these particular broad-line-profile shapes. Given the result that smaller BLR sizes produce smaller values of $\log_{10}(\mathrm{FWHM}/\sigma)$, and our ultimate goal of investigating what BLR geometry and kinematics produce smaller line-profile shapes, the remaining of our CARAMEL model tests will focus solely on BLR sizes with mean radius $\mu = 1$ and minimum radius within the range $F = 0$–0.3.

5.2. BLR Disk Thickness

Next we test whether BLR disk thickness plays a role in determining the Hβ broad-line-profile shape. This idea stems from Pringle (1981), who found that the geometric height of an accretion disk is proportional to the ratio of turbulent velocity to rotational velocity of the disk. And although this notion applies to accretion disks, disk-outflow models, which suggest that the BLR and the obscuring torus are closely connected, possibly forming one continuous structure that feeds/flows from the central accretion disk (e.g., Emmering et al. 1992; Konigl & Kartje 1994; Kartje & Königl 1996; Kishimoto et al. 2011; Koshida 2015), qualify the application to a BLR disk. Thus, as suggested by Kollatschny & Zetzl (2011), BLR lines with smaller values of $\log_{10}(\mathrm{FWHM}/\sigma)$ must have more of a spherical structure.

Using our CARAMEL models, we vary θ_o and F, and keep all other parameters set to the following values: $\theta_i = 25°$, $\beta = 1.0$, $\mu = 1$, $\log_{10}(M_{\mathrm{BH}}/M_\odot) = 7.5$, $f_{\mathrm{flow}} = 0.5$, $f_{\mathrm{ellip}} = 1.0$, $\theta_e = 90°$, $\sigma_{\mathrm{turb}} = 0.001$. Again, this configuration was selected in order to reflect particles on bound circular orbits. As expected, larger opening angles θ_o (i.e., thicker BLR disks) produce broad lines with smaller values of $\log_{10}(\mathrm{FWHM}/\sigma)_{\mathrm{mean}}$ (see Figure 8). The spherical BLR disk represented by $\theta_o = 45°$ even begins to

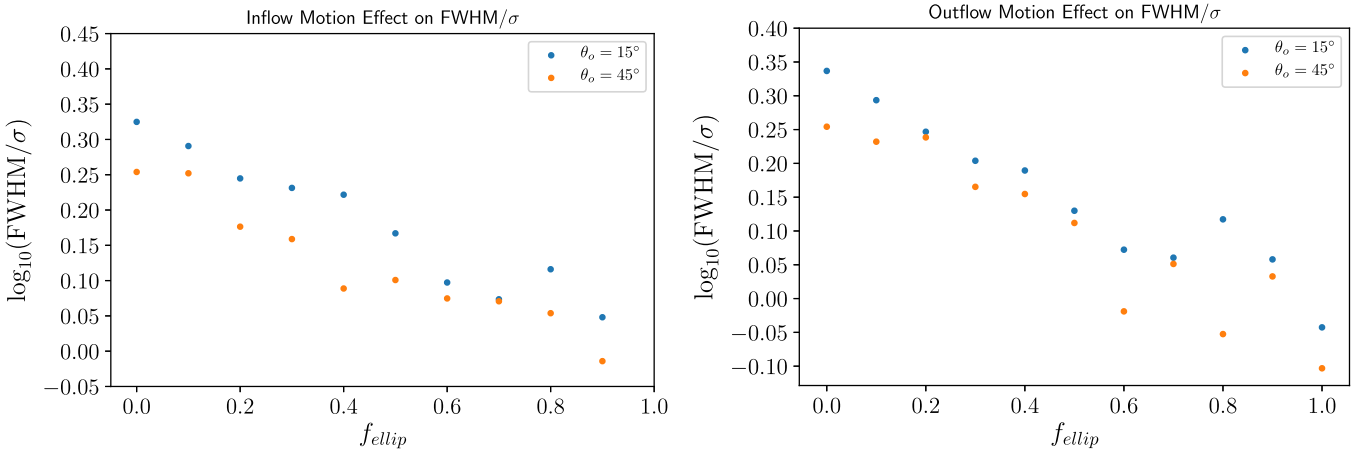

Figure 9. Inflow (left) and outflow (right) effects on line-profile shape. Two different BLR disk thickness/opening angles θ_o are used. In both plots, a thick disk with $\theta_o = 15°$ is shown in blue and a spherical structure with $\theta_o = 45°$ is shown in orange. The x-axis, f_{ellip}, represents the fraction of particles on elliptical orbits. Thus an increasing value of f_{ellip} represents a greater percentage of particles on elliptical orbits, rather than on radially inflowing/outflowing orbits. For both inflowing/outflowing motion, we see that line profiles with smaller values of $\log_{10}(\mathrm{FWHM}/\sigma)_{mean}$ are produced with most of the particles on elliptical orbits with some inflow/outflow motion. Additionally, our results reconfirm our finding with thick diskness, a more spherical BLR produces broad lines with smaller values of $\log_{10}(\mathrm{FWHM}/\sigma)_{mean}$, and confirm that inflowing/outflowing BLR motion is able to produce the line-profile shapes we are particularly interested in, e.g., $\log_{10}(\mathrm{FWHM}/\sigma) < 0.2$.

have a line-profile shape defined by $\log_{10}(\mathrm{FWHM}/\sigma) \approx 0.2$, with bound circular orbits (without inflow/outflow and/or turbulent motion).

5.3. Inflow/Outflow Motion

For this test, we vary f_{ellip} (the fraction of particles with elliptical orbits) while keeping all other parameters held constant. The values selected for all other parameters are as follows: $\theta_i = 25°$, $\beta = 1.0$, $\mu = 1$, $\log_{10}(M_{BH}/M_\odot) = 7.5$, $\theta_e = 45°$, $\sigma_{turb} = 0.001$. We use a value of $f_{flow} = 0.1$ for inflow motion, and a value of $f_{flow} = 0.9$ for outflow motion. Additionally, we also use two separate disk thickness parameters for our test, $\theta_o = 15°$ and $\theta_o = 45°$. We remind the reader that $\theta_e = 45°$ and f_{ellip} represent particles on highly elliptical bound orbits (with $1 - f_{ellip}$ on inflowing/outflowing orbits, as determined by the value of f_{flow}). Therefore, a greater value of f_{ellip} represents a greater fraction of particles on elliptical orbits, rather than radially inflowing/outflowing orbits.

We find that inflowing/outflowing kinematics are able to produce broad-line profiles with smaller values of $\log_{10}(\mathrm{FWHM}/\sigma)_{mean}$, i.e., $\log_{10}(\mathrm{FWHM}/\sigma) \approx 0.1$–$0.2$. In some cases, even values corresponding to $\log_{10}(\mathrm{FWHM}/\sigma) < 0.1$ are produced (see Figure 9). These results also validate our previous finding in which flatter structures (e.g., $\theta_o = 15°$) produce broad lines with larger values of $\log_{10}(\mathrm{FWHM}/\sigma)_{mean}$, compared to more spherical structures (e.g., $\theta_o = 45°$), which produce broad lines with smaller values of $\log_{10}(\mathrm{FWHM}/\sigma)_{mean}$. We also see that $\log_{10}(\mathrm{FWHM}/\sigma)$ decreases, with increasing values of f_{ellip}. A value of $f_{ellip} = 0.4$ corresponds to 40% of particles on elliptical orbits, with the remaining 60% on inflowing/outflowing orbits near escape velocity. While a value of $f_{ellip} = 0.9$ corresponds to 90% of particles on elliptical orbits, with the remaining 10% on inflowing/outflowing orbits. This suggests that a combination of inflow/outflow motion and highly elliptical orbits produces broad lines with smaller values of $\log_{10}(\mathrm{FWHM}/\sigma)_{mean}$, rather than pure inflow/outflow motion.

5.4. Turbulent Motion

In addition to inflow/outflow motion, turbulence has also been suggested to cause the extended wings found in a Lorentz profile (Kollatschny & Zetzl 2013). We test the effect of turbulent motion on line-profile shape using the CARAMEL model parameter σ_{turb}, which allows for macroturbulent velocities. Since the random macroturbulent velocity that is added to the line-of-sight velocity of the particles, depends on both σ_{turb} and $|v_{circ}|$, we test with two different values of $\log_{10}(M_{BH}/M_\odot)$, as a larger black-hole mass would result in greater magnitudes of circular velocity, and thus larger random macroturbulent velocities. Hence, we expect a more massive black hole, with greater turbulent motion, to have broad lines with smaller values of $\log_{10}(\mathrm{FWHM}/\sigma)_{mean}$.

For both scenarios, $\log_{10}(M_{BH}/M_\odot) = 7.0$ and $\log_{10}(M_{BH}/M_\odot) = 8.5$, we set particles on mostly bound outflowing orbits ($\theta_e = 45°$ and $f_{flow} = 0.9$) while varying the σ_{turb} parameter within the limits of its prior, 0.001–0.1. As expected, we find the more massive black hole, $\log_{10}(M_{BH}/M_\odot) = 8.5$, produces broad lines with smaller values of $\log_{10}(\mathrm{FWHM}/\sigma)_{mean}$, with increasing macroturbulent contributions (see Figure 10).

6. Conclusions

We use the direct modeling results of a sample of 28 AGNs: nine from LAMP 2016 (V22), seven from LAMP 2011 (W18), four from AGN10 (G17), five from LAMP 2008 (P14), one from AGNSTORM (W20), one from B21, and one from B22. The CARAMEL results of these 28 AGNs provide insight into BLR geometry and kinematics and constrain M_{BH} measurements without implementing the scale factor f used in reverberation-mapping estimates. The cross-correlation time lags and line widths reported by each subsample's respective reverberation-mapping paper are employed to determine individual scale factors for each source. Using the extended sample described above, we search for existing correlations between scale factor and other AGN/BLR parameters/observables. Our main results are as follows.

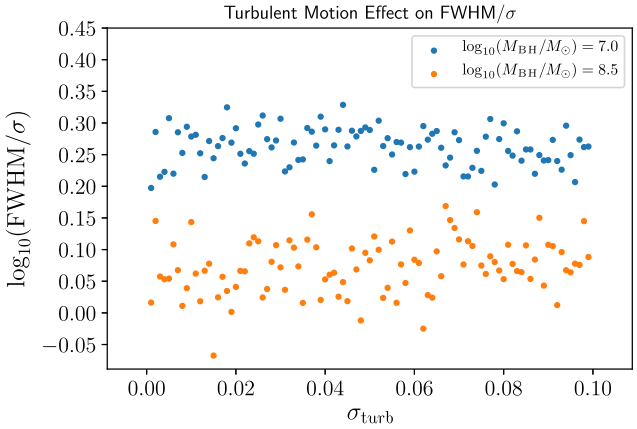

Figure 10. We investigate the role of turbulent motion in line-profile shape using CARAMEL toy models by varying the parameter $\sigma_{\rm turb}$, and holding all other model parameters constant. Since macroturbulent velocities depend on both $\sigma_{\rm turb}$ and $|v_{\rm circ}| \propto \log_{10}(M_{\rm BH}/M_{\odot})$, we test the effects of turbulent motion using two different black-hole masses. The blue points correspond to $\log_{10}(M_{\rm BH}/M_{\odot}) = 7.0$ and the orange points correspond to $\log_{10}(M_{\rm BH}/M_{\odot}) = 8.5$. As expected, we see the more massive black hole, which represents greater turbulent motion, produces broad lines with smaller values of $\log_{10}({\rm FWHM}/\sigma)_{\rm mean}$.

1. We find 3.4σ evidence for a correlation between $\log_{10}(f_{{\rm mean},\sigma})$ and black-hole mass.
2. We find 2.8σ marginal evidence for a correlation between $\log_{10}(f_{{\rm rms},\sigma})$ and black-hole mass.
3. We find 2.1σ marginal evidence for an anticorrelation between $\log_{10}(f_{\rm mean,FWHM})$ and BLR disk thickness.
4. We find 2.4σ marginal evidence for an anticorrelation between $\log_{10}(f_{\rm rms,FWHM})$ and BLR disk thickness.
5. We find 2.6σ marginal evidence for an anticorrelation between $\log_{10}(f_{\rm mean,FWHM})$ and BLR inclination angle.
6. We find 2.4σ marginal evidence for an anticorrelation between $\log_{10}(f_{{\rm rms},\sigma})$ and BLR inclination angle.
7. We find 2.0σ marginal evidence for an anticorrelation between $\log_{10}(f_{{\rm mean},\sigma})$ and BLR inclination angle.
8. We find 2.2σ marginal evidence for a correlation between line-profile shape measured from the rms spectrum, $\log_{10}({\rm FWHM}/\sigma)_{\rm rms}$, and $\log_{10}(f_{{\rm rms},\sigma})$.
9. We investigate how BLR properties may effect measured line-profile shape using CARAMEL models, and find that smaller BLR size, spherical geometries, inflow/outflow motion, and turbulent motion produce broad lines with smaller values of $\log_{10}({\rm FWHM}/\sigma)_{\rm mean}$.
10. We conclude that these geometric & kinematic effects cause a larger observed sigma line width (and cuspier FWHM/σ) at fixed $M_{\rm BH}$, requiring a smaller virial factor, f, for black-hole mass estimators.

The sources modeled by V22 have increased the number of AGNs with dynamical modeling of the BLR by nearly 50% and led to the discovery of a correlation with the scale factor and line-profile shape. The correlation with line-profile shape may provide an observational proxy for the virial coefficient in the future, however, further CARAMEL studies and a larger sample are needed to confirm the statistical significance of the correlation.

We thank the anonymous referee for their helpful comments and suggestions, which significantly improved this manuscript. L.V., P.R.W., and T.T. acknowledge support from the NSF through grant AST-1907208, "Collaborative Research: Establishing the Foundations of Black Hole Mass Measurements of AGN across Cosmic Time."

Research at UC Irvine has been supported by NSF grants AST-1907290. V.U. acknowledges funding support from the University of California Riverside's Chancellor's Postdoctoral Fellowship and NASA Astrophysics Data Analysis Program grant #80NSSC20K0450. T.T. acknowledges support by the Packard Foundation through a Packard research fellowship. V. N.B. gratefully acknowledges assistance from NSF Research at Undergraduate Institutions (RUI) grants AST-1312296 and AST-1909297. Note that findings and conclusions do not necessarily represent views of the NSF. D.C.L.'s group at San Diego State University gratefully acknowledges support from the NSF through grants AST-1210311 and AST-2010001.

M.C.B. gratefully acknowledges support from the NSF through grant AST-2009230. G.C. acknowledges NSF support under grant AST-1817233. J.H.W. acknowledges funding from the Basic Science Research Program through the National Research Foundation of Korean Government (NRF-2021R1A2C3008486). A.V.F.'s group at U.C. Berkeley is grateful for support from the TABASGO Foundation, the Christopher R. Redlich Fund, the Miller Institute for Basic Research in Science (in which he was a Miller Senior Fellow), and many individual donors. We acknowledge the generous support of Marc J. Staley, whose fellowship partly funded B.E.S. while contributing to the work presented here in as a graduate student.

This research has made use of the NASA/IPAC Extragalactic Database (NED), which is operated by the Jet Propulsion Laboratory, California Institute of Technology, under contract with the National Aeronautics and Space Administration.

Appendix
CARAMEL Code Modifications

The minor modifications made to the original CARAMEL code, after its use by W18, G17, P14, W20, B21, and B22, (and prior to the use by V22) are outlined in the Appendix of Williams & Treu (2022). Here we summarize the content found in Williams & Treu (2022).

The original CARAMEL model used by W18, G17, P14, W20, B21, and B22 first draws the particles' radii from a shifted gamma distribution as described in the text. Then the particles are placed on the positive x-axis and each particle is rotated around the z-axis, by an angle drawn from a uniform distribution between 0 and 2π. The particles are then rotated about the y-axis, by an angle drawn from the distribution $\arccos(\cos\theta_o + (1 - \cos\theta_o) \times U^{\gamma})$, where $\theta_{\rm o}$ determines the opening angle (disk thickness) of the BLR and U is a uniform distribution defined between 0 and 1. Additionally, in this original version of the code, γ is allowed to range from 1 to 5. Upon this second rotation, the particles are rotated twice more: once about the z-axis by an angle drawn from a uniform distribution between 0 and 2π (which creates the thick disk) and once more about the y-axis by an angle defined by $\pi - \theta_{\rm i}$.

Prior to the CARAMEL modeling of the LAMP 2016 sample, our team discovered that the second rotation about the z-axis redacted the effect of γ and modified the CARAMEL code to allow for the effects of γ. The modified version of CARAMEL used by V22 varies from the placement of particles from the shifted gamma distribution. Rather than place all particles on the positive x-axis as described above, particles are placed on

both positive and negative sides of the x-axis. Then the particles are only rotated a total of three times, rather than four. The first rotation is about the y-axis, rather than the z-axis, and is defined by an angle drawn from the distribution $\arcsin(\sin\theta_o \times U^{1/\gamma})$, which creates a double wedge in the xz plane. After the first rotation, the particles are then rotated about the z-axis by an angle drawn from a uniform distribution between 0 and 2π (which creates a thick disk). Then, the particles are rotated by one final rotation about the y-axis by an angle defined by $\pi - \theta_i$.

After the changes made in geometric construction, we noticed that most of the effects of γ occur within the ranges $\gamma = 1$–2, and changed the priors on the parameter accordingly.

ORCID iDs

Lizvette Villafaña https://orcid.org/0000-0002-1961-6361
Peter R. Williams https://orcid.org/0000-0002-4645-6578
Tommaso Treu https://orcid.org/0000-0002-8460-0390
Aaron J. Barth https://orcid.org/0000-0002-3026-0562
Vivian U https://orcid.org/0000-0002-1912-0024
Vardha N. Bennert https://orcid.org/0000-0003-2064-0518
Hengxiao Guo https://orcid.org/0000-0001-8416-7059
Misty C. Bentz https://orcid.org/0000-0002-2816-5398
Gabriela Canalizo https://orcid.org/0000-0003-4693-6157
Alexei V. Filippenko https://orcid.org/0000-0003-3460-0103
Elinor Gates https://orcid.org/0000-0002-3739-0423
Michael D. Joner https://orcid.org/0000-0003-0634-8449
Matthew A. Malkan https://orcid.org/0000-0001-6919-1237
Jong-Hak Woo https://orcid.org/0000-0002-8055-5465
Bela Abolfathi https://orcid.org/0000-0003-1820-8486
Thomas Bohn https://orcid.org/0000-0002-4375-254X
K. Azalee Bostroem https://orcid.org/0000-0002-4924-444X
Thomas G. Brink https://orcid.org/0000-0001-5955-2502
Maren Cosens https://orcid.org/0000-0002-2248-6107
Goni Halevi https://orcid.org/0000-0002-7232-101X
Carol E. Hood https://orcid.org/0000-0003-0034-5909
Douglas C. Leonard https://orcid.org/0000-0001-7839-1986
Raúl Michel https://orcid.org/0000-0003-1263-808X
Daeseong Park https://orcid.org/0000-0001-9877-1732
Jordan N. Runco https://orcid.org/0000-0003-4852-8958
Remington O. Sexton https://orcid.org/0000-0003-3432-2094
Chance L. Spencer https://orcid.org/0000-0002-4202-4188
Benjamin E. Stahl https://orcid.org/0000-0002-3169-3167
Jonelle L. Walsh https://orcid.org/0000-0002-1881-5908
WeiKang Zheng https://orcid.org/0000-0002-2636-6508

References

Agudo, I., Gómez, J. L., Casadio, C., Cawthorne, T. V., & Roca-Sogorb, M. 2012, ApJ, 752, 92
Barth, A. J., Bennert, V. N., Canalizo, G., et al. 2015, ApJS, 217, 26
Batiste, M., Bentz, M. C., Raimundo, S. I., Vestergaard, M., & Onken, C. A. 2017, ApJL, 838, L10
Bennert, V. N., Treu, T., Woo, J.-H., et al. 2010, ApJ, 708, 1507
Bentz, M. C., Denney, K. D., Cackett, E. M., et al. 2006, ApJ, 651, 775
Bentz, M. C., Street, R., Onken, C. A., & Valluri, M. 2021a, ApJ, 906, 50
Bentz, M. C., Williams, P. R., Street, R., et al. 2021b, ApJ, 920, 112
Bentz, M. C., Williams, P. R., & Treu, T. 2022, ApJ, 934, 168
Blandford, R. D., & McKee, C. F. 1982, ApJ, 255, 419
Cackett, E. M., Bentz, M. C., & Kara, E. 2021, iSci, 24, 102557
Collin, S., Kawaguchi, T., Peterson, B. M., & Vestergaard, M. 2006, A&A, 456, 75
Denney, K. D., Peterson, B. M., Pogge, R. W., et al. 2010, ApJ, 721, 715
Ding, X., Silverman, J., Treu, T., et al. 2020, ApJ, 888, 37
Emmering, R. T., Blandford, R. D., & Shlosman, I. 1992, ApJ, 385, 460
Ferrarese, L., & Ford, H. 2005, SSRv, 116, 523
Ferrarese, L., & Merritt, D. 2000, ApJL, 539, L9
Gebhardt, K., Bender, R., Bower, G., et al. 2000, ApJL, 539, L13
Goad, M. R., Korista, K. T., & Ruff, A. J. 2012, MNRAS, 426, 3086
Graham, A. W., Onken, C. A., Athanassoula, E., & Combes, F. 2011, MNRAS, 412, 2211
Gravity Collaboration, Amorim, A., Bauböck, M., et al. 2020, A&A, 643, A154
Gravity Collaboration, Sturm, E., Dexter, J., et al. 2018, Natur, 563, 657
Grier, C. J., Martini, P., Watson, L. C., et al. 2013, ApJ, 773, 90
Grier, C. J., Pancoast, A., Barth, A. J., et al. 2017, ApJ, 849, 146
Grier, C. J., Peterson, B. M., Pogge, R. W., et al. 2012, ApJ, 755, 60
Jorstad, S. G., Marscher, A. P., Lister, M. L., et al. 2005, AJ, 130, 1418
Kartje, J. F., & Königl, A. 1996, VA, 40, 133
Kelly, B. C. 2007, ApJ, 665, 1489
Kishimoto, M., Hönig, S. F., Antonucci, R., et al. 2011, A&A, 536, A78
Kollatschny, W., & Zetzl, M. 2011, BaltA, 20, 400
Kollatschny, W., & Zetzl, M. 2013, A&A, 549, A100
Konigl, A., & Kartje, J. F. 1994, ApJ, 434, 446
Kormendy, J., & Ho, L. C. 2013, ARA&A, 51, 511
Kormendy, J., & Richstone, D. 1995, ARA&A, 33, 581
Koshida, S. 2015, TORUS2015: The AGN Unification Scheme After 30 Years, ed. P. Gandhi & S. F. Hoenig
Magorrian, J., Tremaine, S., Richstone, D., et al. 1998, AJ, 115, 2285
Onken, C. A., Ferrarese, L., Merritt, D., et al. 2004, ApJ, 615, 645
Pancoast, A., Brewer, B. J., & Treu, T. 2011, ApJ, 730, 139
Pancoast, A., Brewer, B. J., Treu, T., et al. 2014, MNRAS, 445, 3073
Park, D., Kelly, B. C., Woo, J.-H., & Treu, T. 2012a, ApJS, 203, 6
Park, D., Woo, J.-H., Treu, T., et al. 2012b, ApJ, 747, 30
Pei, L., Fausnaugh, M. M., Barth, A. J., et al. 2017, ApJ, 837, 131
Peterson, B. M. 1993, PASP, 105, 247
Peterson, B. M., Ferrarese, L., Gilbert, K. M., et al. 2004, ApJ, 613, 682
Pringle, J. E. 1981, ARA&A, 19, 137
Salviander, S., Shields, G. A., Gebhardt, K., & Bonning, E. W. 2007, ApJ, 662, 131
Schulze, A., & Wisotzki, L. 2011, A&A, 535, A87
Shen, Y. 2013, BASI, 41, 61
Shields, G. A., & Salviander, S. 2009, in ASP Conf. Ser. 419, Galaxy Evolution: Emerging Insights and Future Challenges, ed. S. Jogee et al. (San Francisco, CA: ASP), 392
Targett, T. A., Dunlop, J. S., & McLure, R. J. 2012, MNRAS, 420, 3621
Treu, T., Malkan, M. A., & Blandford, R. D. 2004, ApJL, 615, L97
U, V., Barth, A. J., Vogler, H. A., et al. 2022, ApJ, 925, 52
Villafaña, L., Williams, P. R., Treu, T., et al. 2022, ApJ, 930, 52
Williams, P. R., Pancoast, A., Treu, T., et al. 2018, ApJ, 866, 75
Williams, P. R., Pancoast, A., Treu, T., et al. 2020, ApJ, 902, 74
Williams, P. R., & Treu, T. 2022, ApJ, 935, 128
Woo, J.-H., Schulze, A., Park, D., et al. 2013, ApJ, 772, 49
Woo, J.-H., Treu, T., Barth, A. J., et al. 2010, ApJ, 716, 269
Woo, J.-H., Treu, T., Malkan, M. A., & Blandford, R. D. 2006, ApJ, 645, 900
Woo, J.-H., Treu, T., Malkan, M. A., & Blandford, R. D. 2008, ApJ, 681, 925
Woo, J.-H., Yoon, Y., Park, S., Park, D., & Kim, S. C. 2015, ApJ, 801, 38